Automatic Nuclei Detection based on Generalized Laplacian of Gaussian Filters

Hongming Xu, Cheng Lu, Richard Berendt, Naresh Jha, and Mrinal Mandal, *Senior Member, IEEE*

Abstract—Efficient and accurate detection of cell nuclei is an important step towards automatic analysis in histopathology. In this work, we present an automatic technique based on generalized Laplacian of Gaussian (gLoG) filter for nuclei detection in skin histopathological images. The proposed technique first generates a bank of gLoG kernels with different scales and orientations, and then performs convolution between directional gLoG kernels and the candidate image to obtain a set of response maps. The local maxima of response maps are detected and clustered into different groups by mean-shift algorithm based on their geometrical closeness. The point which has the maximum response in each group is finally selected as the nucleus seed. Experimental results on 12 large images with 7701 nuclei show that the proposed technique provides a superior performance in nuclei detection compared to existing techniques.

Index Terms—Nuclei detection, Laplacian of Gaussian filter, mean-shift algorithm, thresholding

I. INTRODUCTION

ROBUST nuclei detection is an important step in histopathology, as the counts of nuclei provide quantitative information when studying changes in cells, tissues and organs [1, 2]. In addition, nuclei detection is usually the first step for nuclei segmentation [3, 4], and the accuracy of segmentation depends critically on the accuracy and reliability of the detected points (i.e., seed points) [5].

With recent advances in digital imaging and machine intelligence, enormous research efforts have been devoted to the development of automatic nuclei detection and segmentation [6, 7]. Thresholding-based techniques have been widely used for identifying nuclei numbers and locations [8, 9], but they have limitations in locating clustered nuclei. In order to detect clustered nuclei, several works based on H-minima transform and radial voting have been developed. Cheng et al. [10] proposed an adaptive H-minima transform technique that detects nuclei by adaptively suppressing the local minima from the inner distance map. Jung et al. [11] further formulated the nuclei detection based on H-minima transform as an optimization problem, which determines an optimal depth value (corresponds to the minimum fitting error) to suppress

H. Xu and M. Mandal are with the Department of Electrical and Computer Engineering, University of Alberta, Edmonton, AB, T6G 2V4 Canada (e-mail: mxu@ualberta.ca, mmandal@ualberta.ca).

C. Lu is with the College of Computer Science, Shaanxi Normal University, Xi'an, 710062 Shaanxi, China. C. Lu is supported by the National Natural Science Foundation of China (Grant No.61401263) and Natural Science Basic Research Plan in Shaanxi Province of China (Program No.2015JQ6228) (e-mail: chenglu@snnu.edu.cn).

R. Berendt and N. Jha are with the Department of Oncology, Cross Cancer Institute, University of Alberta, Edmonton, AB, T6G 1Z2 Canada (e-mail: richard.berendt@albertahealthservices.ca, naresh.jha@albertahealthservices.ca).
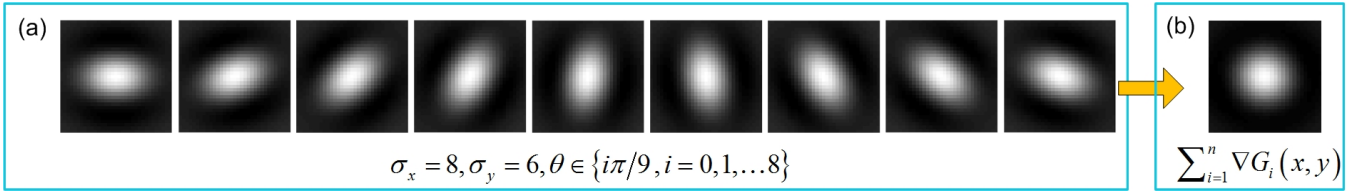
the undesired local minima in the distance map. Parvin et al. [12] proposed a multi-pass voting technique for inferring the centers of cell nuclei. This technique initially votes along the gradient direction of high gradient pixels in a cone-shape voting area, and then iteratively votes in multiple passes with a shrunk voting area and updated voting direction (towards the highest votes in the previous pass). The points which have the votes above a predefined threshold are finally considered as nuclei seeds. In order to reduce the computational complexity of multiple-pass voting [12], Qi et al. [3] proposed a sing-pass voting based nuclei detection technique, which only performs a single-pass voting followed by mean shift clustering to detect nuclei seeds. Xu et al. [4] furthered improved single-pass voting algorithm by voting along nuclei boundaries and distributing votes with a Gaussian kernel in nuclei regions. Although these techniques have been reported to provide a good performance, they are either sensitive to the predefined parameters or have high computational complexity. They tend to be infeasible for high-throughput analysis of images with a large number of cell nuclei.

Recently, Laplacian of Gaussian (LoG) filter based techniques have been introduced for cells and nuclei detection. Byun et al. [1] proposed a nuclei detector in retinal images that is designed based on the Laplacian-of-Gaussian (LoG) filter at a fixed scale (set empirically). Although this method has the advantage of low computational complexity, it fails to provide a good performance when the candidate image has nuclei with different sizes and shapes. Al-Kofahi et al. [13] proposed a multi-scale Laplacian of Gaussian (mLoG) based technique, which first extracts image foreground with a graph-cuts-based binarization, and then detects nuclei seeds by mLoG filtering with a distance-map-constrained adaptive scale selection. The mLoG filter is efficient in locating the centers of 2-D near-circular blobs but has limitations in detecting blobs with general elliptical shapes. Kong et al. [14] proposed a gLoG filter based algorithm for detecting general elliptical blob structures (like cell nuclei) in images. This algorithm first generates a set of log-scale-normalized gLoG kennels, $\nabla G_i(x, y), i = 1 \ldots L$, with different scales and orientations. The convolution between each gLoG kernel and the image is then performed, and an aggregated response map R_s is obtained by summing up all response maps, i.e.,

$$R_s = \sum_{i=1}^{L} (\nabla G_i(x, y) * I) \qquad (1)$$

where $*$ is the convolution operation, I is the image and L is the number of gLoG kernels. The local maxima in the

Fig. 1. Summation of gLoG kernels. (a) 9 directional gLoG kernels. (b) The summation result. Note that σ_x and σ_y are the scales of a gLoG kernel, and θ is the direction of a gLoG kernel.

aggregated response map R_s are finally detected as nuclei seeds. Note that Eq. (1) can be reformulated, based on the distributivity property of the convolution operation [15], as:

$$R_s = I * \sum_{i=1}^{L} \nabla G_i(x, y) \qquad (2)$$

The computational complexity of Eq. (2) is much lower than that of Eq. (1), as the times of convolution operations have been greatly reduced (from L to 1). Actually, the summation of different directional gLoG kernels together, like in Eq. (2), essentially results in a LoG kernel. For example, Fig. 1(a) shows a set of 9 directional gLoG kernels with scales $\sigma_x = 8$ and $\sigma_y = 6$. Fig. 1(b) shows the summation of gLoG kernels in Fig. 1(a), which is essential a LoG kernel. Thus the directional information of gLoG kernels have been lost during the generation of the aggregated response map by Eq. (1) in [14]. Since the blob location algorithm in [14] have not taken the advantage of gLoG kernels's directional information, it is likely to miss seeds for nuclei regions that do not have peak responses in the aggregated response map R_s. Besides, the algorithm in [14] is quite sensitive to the local noise in the image background [16], as it considers all local maxima of the response map R_s as nuclei seeds. Fig. 2 shows an example of nuclei detection in a hematoxylin and eosin (H&E) stained skin image using the algorithm in [14], where the automatically detected nuclei seeds are indicated by (green) plus symbols. Note that the (red) rectangles highlight the missed nuclei (without seeds), while the (blue) circles highlight the false seeds (due to noisy pixels).
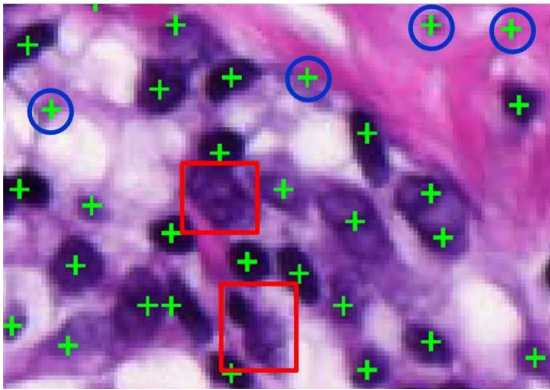

Fig. 2. Nuclei detection results by the algorithm in [14]. Note that (green) plus symbols indicate the detected nuclei, whereas (red) rectangles and (blue) circles highlight the missed nuclei and false seeds, respectively.

In this paper, we propose an efficient and accurate technique for nuclei detection in microscopic images, which overcomes many of the limitations of the existing techniques. The main contribution of this work is that a computationally efficient nuclei seeds detection algorithm based on directional gLoG kernels and mean-shift clustering is proposed. This algorithm searches nuclei seeds from multiple response maps obtained by convolving directional gLoG kernels with the image. False seeds in the image background are removed based on adaptive thresholding, and redundant seeds are merged based on mean-shift clustering. The organization of this paper is as follows. Section II illustrates image dataset used in this work. Section III describes the proposed technique, followed by the performance evaluations in Section IV. The conclusion is presented in Section V.

II. DATASET DESCRIPTION

This study was based on histopathological images obtained from formalin-fixed paraffin-embedded tissue blocks of skin biopsies. The histological sections of skin tissues are about $4\mu m$ thick each and are stained with H&E using automated stainer. The skin biopsies contained melanocytic nevi and skin melanomas. The original whole slide skin images were captured under 40X magnification on Carl Zeiss MIRAX MIDI Scanning system. The dataset used in this work consists of 12 different skin histopathological images, which were cropped from six whole slide images. These cropped images were saved in TIFF format with 10X magnification using MIRAX Viewer software. The 10X magnification is selected for a good balance between image quality and size. The 12 images on average have a size of 1326×667 pixels, and have a total of 7,701 cell nuclei. Although the dataset consists of colored images, this work uses the red channel image, as it provides a good contrast between nuclei and background in the H&E stained image [9, 17].

III. PROPOSED TECHNIQUE

The schematic of the proposed technique for nuclei detection is shown in Fig. 3. It is observed that there are three modules. In the first module, a bank of log-scale-normalized gLoG kernels with different scales and orientations are constructed. In the second module, the constructed gLoG kernels are summed together according to their orientations, and the response maps are generated by convolving the summed gLoG kernels with the image. In the third module, the nuclei seeds are detected from multiple response maps with redundant detections merged by mean-shift clustering. The details of three modules are now presented in the following.
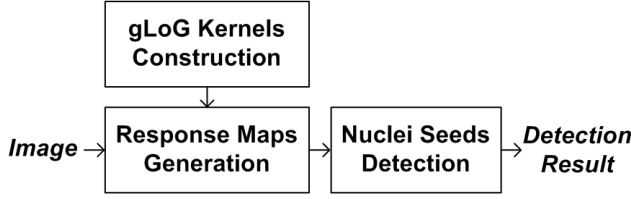
Fig. 3. Schematic of the proposed technique.

A. gLoG Kernels Construction

Because cell nuclei in skin histopathological images typically have circular or elliptical shape, the gLoG kernels (see Fig. 1) are appropriate for nuclei detection. In this work, we use a bank of gLoG kernels with different scales and orientations for subsequent nuclei identification. The gLoG kernel $\nabla^2 G(x,y)$ is given as follows [14]:

$$\nabla^2 G(x,y) = \frac{\partial^2 G(x,y)}{\partial x^2} + \frac{\partial^2 G(x,y)}{\partial y^2} \qquad (3)$$

where (x,y) are the image domain coordinates, $G(x,y) = \lambda \cdot e^{-\left(ax^2 + 2bxy + cy^2\right)}$, and the Laplacian $\partial^2 G(x,y)/\partial x^2$, $\partial^2 G(x,y)/\partial y^2$ are given by:

$$\frac{\partial^2 G(x,y)}{\partial x^2} = \left[(2ax + 2by)^2 - 2a\right] G(x,y) \qquad (4)$$

$$\frac{\partial^2 G(x,y)}{\partial y^2} = \left[(2bx + 2cy)^2 - 2c\right] G(x,y) \qquad (5)$$

where λ is a normalization factor and the parameters a, b, c control the shape and orientation of the gLoG kernel, which are defined as follows:

$$a = \frac{\cos^2\theta}{2\sigma_x^2} + \frac{\sin^2\theta}{2\sigma_y^2} \qquad (6)$$

$$b = -\frac{\sin 2\theta}{4\sigma_x^2} + \frac{\sin 2\theta}{4\sigma_y^2} \qquad (7)$$

$$c = \frac{\sin^2\theta}{2\sigma_x^2} + \frac{\cos^2\theta}{2\sigma_y^2} \qquad (8)$$

where (σ_x, σ_y) are the scales and θ is the orientation of the gLoG kernel. When applying gLoG kernels on the image containing blobs with general elliptical shapes, it produces a scale-and-orientation selective peak response at the center of each object. This can be considered as a pattern matching process, which matches the predefined gLoG kernels of different scales and orientations to the given image patterns. However, a direct application of gLoG kernels to images of blobs would be unreliable, since the signal amplitude of the gLoG convolution at blob regions decreases monotonically as the scales increase. To solve this problem, the following log-scale-normalized gLoG kernel $\nabla^2 G_n(x,y)$ has been introduced [14]:

$$\nabla^2 G_n(x,y) = (1 + \log(\sigma_x)^\alpha)(1 + \log(\sigma_y)^\alpha)\nabla^2 G(x,y) \qquad (9)$$

where α is a positive number (e.g., $\alpha = 0.5$) which can control the eccentricities of detected blobs.

By varying the scales and orientations, a set of different log-scale-normalized gLoG kernels $\nabla^2 G_n(x,y)$ can be obtained. To construct a bank of gLoG kernels for nuclei identification,

in this work, we first set angles that the gLoG kernel's orientation can take, which is as follows:

$$\theta = \frac{\pi}{k}(i-1), \quad i = 1 \dots k \qquad (10)$$

where k is the number of orientations. The range of scales σ_x and σ_y are then set as positive integers between $\sigma_{\min}$ and $\sigma_{\max}$, where $\sigma_{\min}$ and $\sigma_{\max}$ are determined based on the estimated radius of detected nuclei [18]. Without loss of generality, we assume that $\sigma_x > \sigma_y$. Figs. 4(a)(b) show examples of log-scale-normalized gLoG kernels with scales between $[8,8]$ and $[4,4]$ in 4 directions. As observed in Fig. 4(a), the gLoG kernels are rotational-symmetric when $\sigma_x = \sigma_y$, which are essentially the LoG kernels.

B. Response Maps Generation

After constructing a set of normalized gLoG kernels, the next is to convolve the image with gLoG kernels to obtain response maps which provide information about nuclei numbers and locations. Although it is possible to do the convolution between each gLoG kernel and the image (like the blob localization algorithm in [14]), it is time-consuming due to multiple convolutions. To speed up the algorithm, we make use of distributivity property of convolution operation and compute the summation of gLoG kernels before convolution operation. Specifically, for the rotational symmetric gLoG kernels (see Fig.4(a)), the summed gLoG kernel $\nabla^2 G_s(x,y)$ is given by:

$$\nabla^2 G_s(x,y) = \frac{1}{S_0} \sum_{\sigma=\sigma_{\min}}^{\sigma_{\max}} \nabla^2 G_n(x,y;\sigma) \qquad (11)$$

where S_0 is the number of summed rotational symmetric gLoG kernels. For other general elliptical shapes of gLoG kernels (see Fig.4(b)), the summed gLoG filter $\nabla^2 G_s(x,y;\theta)$ is given by:

$$\nabla^2 G_s(x,y;\theta) = \frac{1}{S_k} \sum_{\sigma_x=\sigma_{\min}}^{\sigma_{\max}} \sum_{\sigma_y=\sigma_{\min}}^{\sigma_x} \nabla^2 G_n(x,y;\sigma_x,\sigma_y,\theta) \qquad (12)$$

where S_k is the number of summed elliptical gLoG kernels. Note that $\nabla^2 G_s(x,y;\theta)$ is the summation of gLoG kernels in the orientation θ. Figs. 4(c)(d) show the corresponding summed results of gLoG kernels. With k orientations, there are $k+1$ summed gLoG kernels in total. For brevity, let us denote the summed gLoG kernels as $\nabla^2 G_s^j(x,y)$, where $j = 0 \dots k$. The response image $L^j(x,y)$ is then obtained as:

$$L^j(x,y) = \overline{I}(x,y) * \nabla^2 G_s^j(x,y) \qquad (13)$$

where $*$ is the convolution operator, $I(x,y)$ is the original red channel image and $\overline{I}(x,y) = 255 - I(x,y)$. Note that the nuclei regions appear as dark blobs in the original red channel image, and hence the complement operation in Eq. (13) is performed to make nuclei regions as bright foreground. The response image $L^j(x,y)$ corresponds to the pattern matching result between the image and the gLoG kernel $\nabla^2 G_s^j(x,y)$.

Using $k+1$ normalized gLoG kernels, there are $k+1$ response images obtained by Eq. (13). Fig. 5(a) shows a cropped nucleus with an elliptical shape and a (major axis)
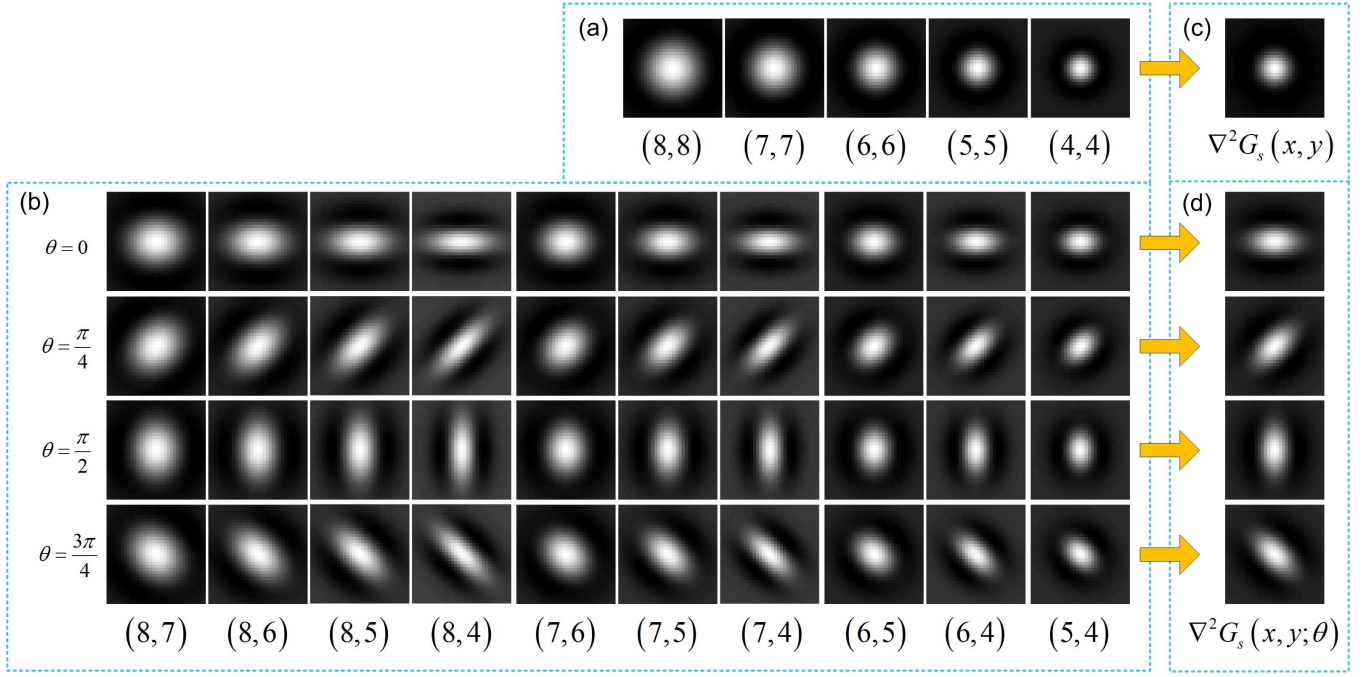
Fig. 4. Example of log-scale-normalized gLoG kernels (with $\alpha = 1$ and $k = 4$). (a) Rotational symmetric LoG kernels with $\sigma_x = \sigma_y \in \{8, 7, 6, 5, 4\}$. (b) gLoG kernels with $\theta \in \{0°, 45°, 90°, 135°\}$, $\sigma_x \in \{8, 7, 6, 5\}$, $\sigma_y \in \{7, 6, 5, 4\}$ and $\sigma_x > \sigma_y$. (c) $\nabla^2 G_s(x, y)$ (see Eq. (11)). (d) $\nabla^2 G_s(x, y; \theta)$ (see Eq. (12)). Note that in (a) and (b) $(\cdot, \cdot)$ corresponds to (σ_x, σ_y).

direction of about $135°$, while Figs. 5(b)-(f) show the response maps obtained by convolving Fig. 5(a) with gLoG kernels in Figs. 4(c)(d), respectively. In Figs. 5(b)-(f) the local maxima (usually round nuclei centers) are also searched and superimposed on the image with (black) plus symbols. As observed in Fig. 5, only the response map (f) provides a local maxima response which indicates a correct detection of the nucleus, while no nuclei are detected from other response maps. Fig. 5(f) provides a correct detection, mainly because the gLoG kernel used in (f) has a similar direction with the nucleus in (a). More details about searching nuclei seeds from multiple response maps will be presented in the next section.
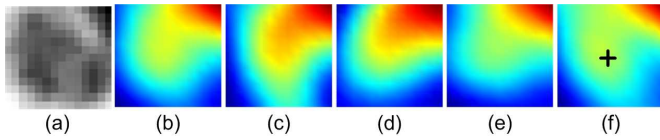

Fig. 5. Response maps. (a) A cropped nucleus. (b)-(f) Color response maps obtained by convolving (a) with gLoG kernels in Figs. 4(c)(d), respectively. Note that (f) has a local maxima response indicated by + symbol, while no local maxima are detected from other response maps.

C. Nuclei Seeds Detection

Using the above obtained response maps $L^j(x, y)$, nuclei seeds can be detected as the points of local maxima which are usually around nuclei centers. In this module, we present the process of determining nuclei seeds from multiple response maps, which consists of four main steps as follows.

Step1: The local maxima of each response image $L^j(x, y)$ are detected. Let us denote them as $\{B_i\}_{i=1...M}$, where M is

the number of local maxima in $k+1$ response maps. Fig. 6(a) shows the image $I(x, y)$ overlapped with local maxima (red + symbols).

Step 2: An adaptive thresholding based technique [4] is first performed on the image $I(x, y)$ to generate a binary mask b_1, where nuclei pixels are represented as binary foreground (binary 1). The local maxima $\{B_i\}_{i=1...M}$, which are in the background of mask b_1 are then eliminated, as they are generated due to the local noise in the image background. Let us denote the local maxima after this step as $\{B_i\}_{i=1...N}$, where N is the number of local maxima. In Fig. 6(a), the local maxima generated due to the local noise are highlighted by the (blue) circles. Fig. 6(b) shows the image $I(x, y)$ with local maxima $\{B_i\}_{i=1...N}$. Note that in Fig. 6(b) the (green) contours of nuclei regions are obtained after image binarization by adaptive thresholding.

Step 3: As observed in 6(b), there are usually more then one point of local maxima for each nuclei region. In other words, it exists the redundant detections of cell nuclei by searching local maxima from multiple response maps. But it is also noted that the local maxima corresponding to each nucleus usually cluster together with a close geometrical distance. In this step, we apply the mean-shift algorithm [19] on N local maxima points $\{B_i\}_{i=1...N}$ and cluster them based on their geometric closeness such that each nucleus corresponds to one cluster of local maxima. Let the number of clusters be denoted by p, and the p clusters be denoted by $\mathcal{T}_l, 1 \leq l \leq p$, where $\sum_{l=1}^{p} n^l = N$ and n^l is the number of local maxima in the cluster $\mathcal{T}_l$. Note that the bandwidth bw of mean-shift algorithm is determined based on estimated radius of nuclei (e.g., 6 pixels in Fig. 6).
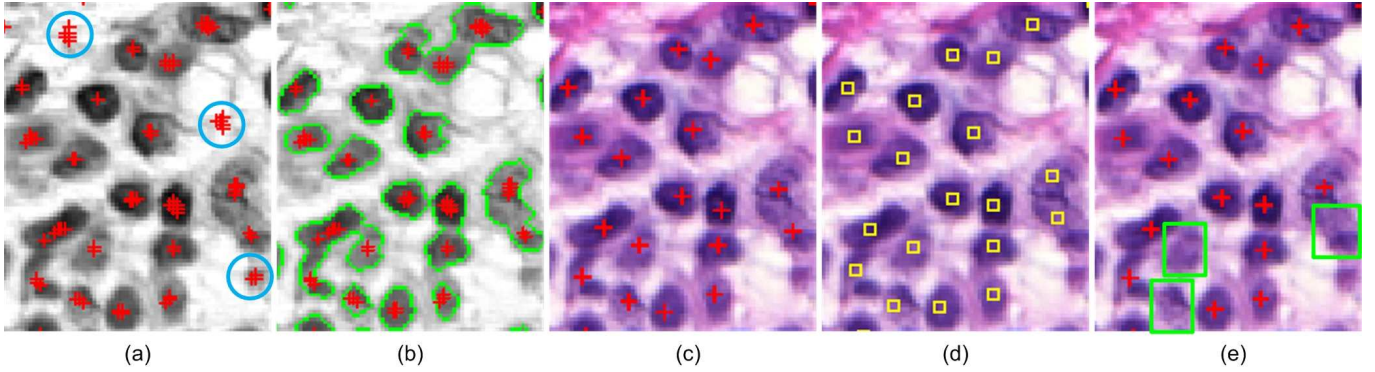
Step 4: Since each nucleus corresponds to one cluster

Fig. 6. Illustration of nuclei detection. (a) $I(x,y)$ with all local maxima (shown as +). (b) $I(x,y)$ with filtered local maxima (shown as +). (c) Original image with detected nuclei seeds by the proposed technique. (d) Original image with ground truths. (e) Original image with detected seeds by the technique in [14]. Note that in (a) the circles indicate the local maxima generated by noise in the image background. In (b) nuclei contours are obtained by image binarization by adaptive thresholding. In (e) the rectangles highlight the missed nuclei (without seeds).

of local maxima, it is necessary to determine one point as nucleus seed. In this work, the point which has the maximum response value (retrieved from the corresponding response image $L^j(x,y)$ obtained in Eq. (13)) is selected as the nuclei seed from each cluster $\mathcal{T}_l, 1 \leq l \leq p$.

Fig. 6(c) shows the original RGB image with the detected nuclei seeds (+ symbols) by the proposed technique, and Fig. 6(d) shows the manually labeled ground truths. Fig. 6(e) shows the original image with nuclei seeds detected by the blob location algorithm in [14], where the missed nuclei are highlighted by rectangles. As observed in Figs. 6(c)(d)(e), the proposed technique provides a more accurate nuclei detection, even for nuclei with light stains. In comparison, the technique in [14] misses several nuclei (i.e., without seeds), which do not have peak responses in the aggregated response map.

IV. EXPERIMENTAL RESULTS

To evaluate the performance of the proposed technique, we carried out a series of experiments using our dataset. The main objective of evaluation is to determine if the automatically detected nuclei seeds are consistent with the manually labeled ground truths. In this section, we present the nuclei detection performance of the proposed technique and compare it with three existing techniques.

A. Parameters Configuration

There are four parameters that should be determined appropriately in the proposed technique. Table I lists the parameters used on our dataset. The parameter k determines the orientations of gLoG kernels, which is set as 9 (i.e., nine orientations: $\theta = m\pi/9, \ m = 0, \ldots, 8$) with an angular resolution of $20°$. The parameters $\sigma_{\min}$ and $\sigma_{\max}$ are determined based on the relationship between the radius r of detected objects and scales of gLoG kernels $\sqrt{2}\sigma_{\min} \leq r \leq \sqrt{2}\sigma_{\max}$ [18]. Here we measure the minimal and maximal radii $(r_{\min}, r_{\max})$ of nuclei (in pixels) in several manually labeled nuclei regions, and set $\sigma_{\min}$ and $\sigma_{\max}$ as $r_{\min}/\sqrt{2}$ and $r_{\max}/\sqrt{2}$, respectively. The bandwidth bw of the mean-shift algorithm is set as the minimal radius $r_{\min}$ of detected objects.

TABLE I
PARAMETERS CONFIGURATION IN THE PROPOSED TECHNIQUE.

Parameters	k	$\sigma_{\min}$	$\sigma_{\max}$	bw
Values	9	4	8	6

We compare the proposed technique with the mLoG based method [13], gLoG based method [14] and voting based method [4]. In the mLoG based method [13], the nuclei regions in the image are first segmented into foreground (binary 1) and an Euclidean distance map is generated. A set of multiple-scale LoG kernels are then applied on the image to generate a response map with scales constrained by the Euclidean distance map. The scale σ of the LoG kernel is the key parameter, which is set as $\sigma = \{4, 5, 6, 7, 8\}$ for multi-scale computation. The gLoG based method [14] has a few key parameters including k, $\sigma_{\min}$ and $\sigma_{\max}$ which are set the same values as our proposed technique (see Table I). However, since the original gLoG based method [14] is highly sensitive to the image noise which cannot be directly applied on our database, we experimentally determines a threshold τ to filter false seeds in the image background. In particular, if the points of local maxima searched from the aggregated response map have a response value above τ, they are considered as nuclei seeds. In this work, τ is set as 45. Figs. 7(a)(b) show the nuclei detection results by the technique in [14] before and after filtering false seeds by the threshold τ. As observed in Fig. 7, the threshold τ can effectively remove false seeds in the image background. In the voting based method [4], the voting radii $[r_{\min}, r_{\max}]$ and the mean-shift bandwidth bw should be adaptive adjusted for different database. In this work, we experimentally set them as $r_{\min} = 4$, $r_{\max} = 15$ and $bw = 6$.

B. Performance Evaluation

To evaluate the nuclei detection performance, the nuclei locations are manually labeled (around nucleus center) using an interactive computer program. These manually labeled nuclei markers are taken as the ground truths. A ground truth seed is considered as a true detection if there exists
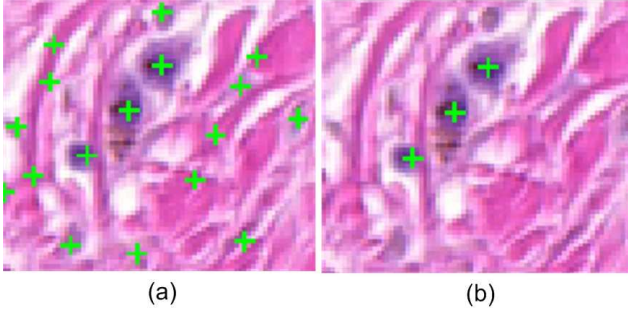
Fig. 7. Nuclei detection results by the technique in [14]. (a) Results before filtering false seeds. (b) Results after filtering false seeds.

an automatic detection within a certain distance d (number of pixels) of it. Similarly, an automatically obtained seed is considered as a false detection if there is not a ground truth seed within a neighborhood of it. Let N_{GT}, N_{DS}, N_{TD} and N_{FD} denote the numbers of ground truth seeds, detected seeds, true detections and false detections, respectively. The performance is evaluated with respect to the true detection rate ($\mathcal{D}_{TDR}$), and false detection rate ($\mathcal{D}_{FDR}$) which are defined as follows:

$$\mathcal{D}_{TDR} = \frac{N_{TD}}{N_{GT}} \times 100\% \tag{14}$$

$$\mathcal{D}_{FDR} = \frac{N_{FD}}{N_{DS}} \times 100\% \tag{15}$$

Table II shows the quantitative evaluations of nuclei detection performance for the proposed technique and existing techniques, where the distance d is set as 6 pixels in computing $\mathcal{D}_{TDR}$ and $\mathcal{D}_{FDR}$. It is observed in Table II that the proposed technique provides a superior performance in true detection rate (on average 92.75%) than all existing techniques. It provides a superior performance in false detection rate (on average 4.92%) than mLoG [13] and gLoG [14] methods, but a similar performance with voting based method [4] (on average 4.53%). Fig. 8 compares nuclei seeds detection performance with respect to $\mathcal{D}_{TDR}$ and $\mathcal{D}_{FDR}$, where the distance d is ranged from 1 to 15 pixels. As observed in Fig. 8, the performance of different techniques is similar when $d < 3$. However, the proposed technique provides a markedly superior performance when $d \geq 3$. The proposed technique makes use of directional information of gLoG kernels and searches potential nuclei seeds from multiple response maps, which provides a more accurate nuclei detection. The similar values of false detection rates between the proposed technique and the voting based method [4] is because both techniques apply mean-shift clustering to detect nuclei seeds, which reduces false positive seeds (e.g., too close seeds are clustered together).

For visual comparison, Fig. 9 shows one randomly cropped image patch with detected nuclei seeds by different techniques. Figs. 9(a)(b)(c) show nuclei detections by the mLoG, gLoG and voting based methods, respectively, whereas Figs. 9(d) shows the result by the proposed technique. Note that in the first row (white) circles highlight a few regions with false detections (e.g., one nucleus has several seeds), and (white)

TABLE II
COMPARISON OF NUCLEI DETECTION PERFORMANCE ($d = 6$).

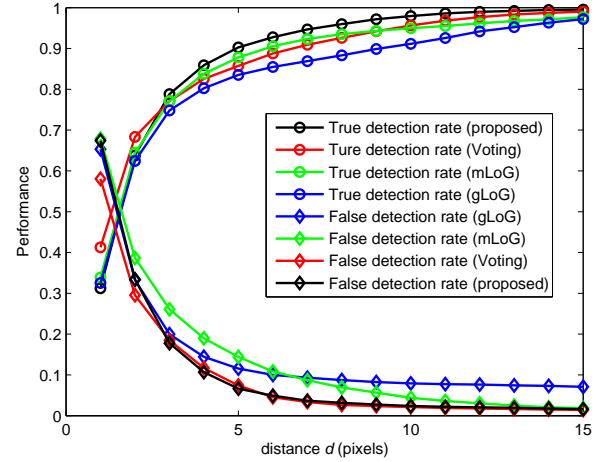| Techniques	N_{GT}	N_{DS}	$\mathcal{D}_{TDR}$(%)	$\mathcal{D}_{FDR}$(%)
mLoG [13]	7701	8332	90.56±1.03	10.85±3.53
gLoG [14]	7701	7052	85.47±5.03	9.99±2.07
Voting [4]	7701	7149	88.76±3.35	4.53±3.35
Proposed	7701	7495	92.75±2.21	4.92±2.51

Fig. 8. Nuclei detection performance with respect to true detection rate and false detection rate.

squares highlight a few regions with missed detections (e.g., nuclei do not have seeds). In the second row (yellow) circles with a radius of 6 pixels are centered at the manually labeled ground truths. As observed in Fig. 9, the proposed technique has lower false and missed detections than existing techniques.

This work is originally motivated by the gLoG based method in [14]. Compared with the blob detection algorithm in [14], the bandwidth bw of mean-shift algorithm is the newly introduced parameter in the proposed technique, which is empirically set as the minimal nuclei radius $r_{\min}$ ($r_{\min} = 6$ in this work). To evaluate the sensitivity of this parameter, we varied bw by 10% and 20% around $r_{\min}$ (or tuned it from 4.8 to 7.2 with a step of 0.6). Fig. 10 shows the true and false detection rates with respect to different bw values. As observed in Fig 10, the true detection rates vary between 91.5% and 94.0%, and the false detection rates vary between 4.8% and 5.0%. From the result in Fig. 10, it can be concluded that the true detection rate is sensitive to the parameter bw, while the false detection rate is robust to choice of the parameter bw.

C. Computational complexity

To evaluate the computational complexity, the average run time over 12 large test images (on average 1326×667 pixels) is calculated. Our experiments were carried out on a 2.9-GHz CPU with 4 GB RAM using MATLAB 2013. Let us denote the average run time as t. Table III shows the values of t for different techniques. As observed in Table III, the voting based technique [4] has the highest computational
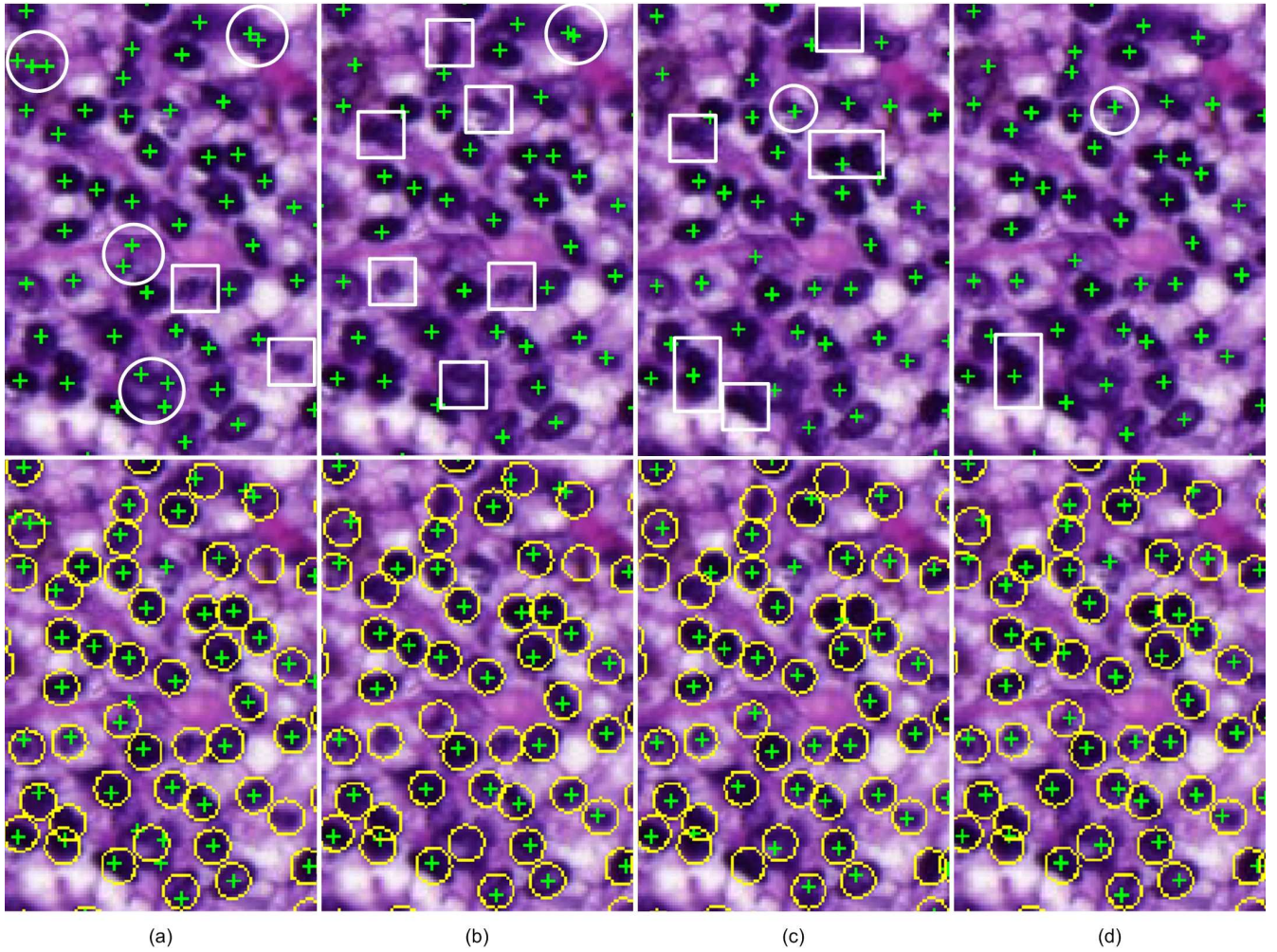
Fig. 9. Nuclei detection results on a representative image patch. (a) mLoG based method [13]. (b) gLoG based method [14]. (c) Voting based method [4]. (d) Proposed technique. Note that the automatically detected nuclei seeds are indicated by + symbols. In the first row the white circles and squares show the regions with false detections and missed detections, respectively. In the second row the yellow circles with a radius of 6 pixels are centered on manually labeled ground truths.
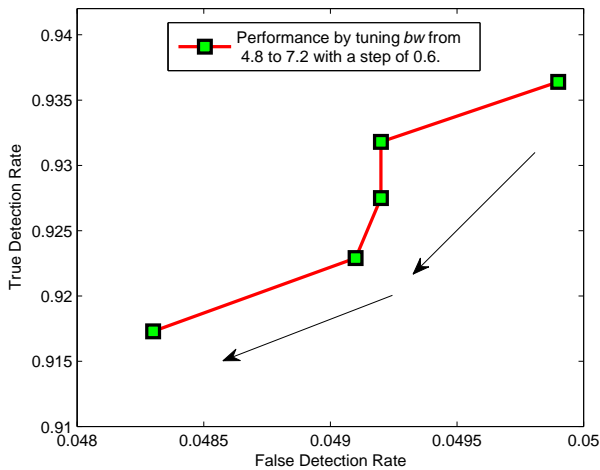

Fig. 10. Performance evaluation by tuning bw from 4.8 to 7.2 with a step of 0.6 (d=6).

complexity (606.36s), while the other techniques roughly have the similar computational complexity. The proposed technique on average takes 11.34s to process an image, which is about three times faster than the gLoG based method (36.25s). This is because we do summations of gLoG kernels according to their orientations before performing convolution operation, which reduces the number of convolutions (convolution takes a relatively long time for a large image).

TABLE III
COMPARISON OF COMPUTATIONAL COMPLEXITY. THE AVERAGE RUN TIME (ART) IS SHOWN IN SECONDS.

ART	mLoG [13]	gLoG [14]	Voting [4]	Proposed
$t(s)$	7.43	36.25	606.36	11.34

V. CONCLUSION

This paper presents a robust nuclei detection technique based on directional gLoG kernels and mean-shift clustering

for microscopic images. The proposed technique first construct a bank of different direction-and-scale gLoG kernels. These gLoG kernels are then summed together according to their orientations and convolved with the image to generate a set of response maps. The nuclei seeds are finally searched from the generated response maps with false seeds removed based on adaptive thresholding and redundant seeds merged based on mean-shift clustering. Experimental results on 7707 nuclei in skin images show that the proposed technique provides a superior performance in nuclei detection compared to existing techniques.

REFERENCES

[1] J. Byun, M. R. Verardo, B. Sumengen, G. P. Lewis, B. Manjunath, and S. K. Fisher, "Automated tool for the detection of cell nuclei in digital microscopic images: application to retinal images," *Mol Vis*, vol. 12, pp. 949–960, 2006.

[2] C. Lu and M. Mandal, "Automated analysis and diagnosis of skin melanoma on whole slide histopathological images," *Pattern Recognition*, vol. 48, no. 8, pp. 2738–2750, 2015.

[3] X. Qi, F. Xing, D. J. Foran, and L. Yang, "Robust segmentation of overlapping cells in histopathology specimens using parallel seed detection and repulsive level set," *IEEE Transactions on Biomedical Engineering*, vol. 59, no. 3, pp. 754–765, 2012.

[4] H. Xu, C. Lu, and M. Mandal, "An efficient technique for nuclei segmentation based on ellipse descriptor analysis and improved seed detection algorithm," *IEEE Journal of Biomedical and Health Informatics*, vol. 18, no. 5, pp. 1729–1741, 2014.

[5] P. Yan, X. Zhou, M. Shah, and S. T. Wong, "Automatic segmentation of high-throughput rnai fluorescent cellular images," *IEEE Transactions on Information Technology in Biomedicine*, vol. 12, no. 1, pp. 109–117, 2008.

[6] H. Fatakdawala, J. Xu, A. Basavanhally, G. Bhanot, S. Ganesan, M. Feldman, J. E. Tomaszewski, and A. Madabhushi, "Expectation–maximization-driven geodesic active contour with overlap resolution (emagacor): Application to lymphocyte segmentation on breast cancer histopathology," *IEEE Transactions on Biomedical Engineering*, vol. 57, no. 7, pp. 1676–1689, 2010.

[7] O. Schmitt and S. Reetz, "On the decomposition of cell clusters," *Journal of Mathematical Imaging and Vision*, vol. 33, no. 1, pp. 85–103, 2009.

[8] S. Petushi, F. U. Garcia, M. M. Haber, C. Katsinis, and A. Tozeren, "Large-scale computations on histology images reveal grade-differentiating parameters for breast cancer," *BMC Medical Imaging*, vol. 6, no. 1, p. 14, 2006.

[9] M. N. Gurcan, T. Pan, H. Shimada, and J. Saltz, "Image analysis for neuroblastoma classification: Segmentation of cell nuclei," in *Proceeding of 28th Annual International Conference on Engineering in Medicine and Biology Society*. IEEE, 2006, pp. 4844–4847.

[10] J. Cheng and J. C. Rajapakse, "Segmentation of clustered nuclei with shape markers and marking function," *IEEE Transactions on Biomedical Engineering*, vol. 56, no. 3, pp. 741–748, 2009.

[11] C. Jung and C. Kim, "Segmenting clustered nuclei using h-minima transform-based marker extraction and contour parameterization," *IEEE Transactions on Biomedical Engineering*, vol. 57, no. 10, pp. 2600–2604, 2010.

[12] B. Parvin, Q. Yang, J. Han, H. Chang, B. Rydberg, and M. H. Barcellos-Hoff, "Iterative voting for inference of structural saliency and characterization of subcellular events," *IEEE Transactions on Image Processing*, vol. 16, no. 3, pp. 615–623, 2007.

[13] Y. Al-Kofahi, W. Lassoued, W. Lee, and B. Roysam, "Improved automatic detection and segmentation of cell nuclei in histopathology images," *IEEE Transactions on Biomedical Engineering*, vol. 57, no. 4, pp. 841–852, 2010.

[14] H. Kong, H. C. Akakin, and S. E. Sarma, "A generalized laplacian of gaussian filter for blob detection and its applications," *IEEE Transactions on Cybernetics*, vol. 43, no. 6, pp. 1719–1733, 2013.

[15] R. Gonzalez and R. Woods, *Digital image processing*, 3rd, Ed. USA: Prentice Hall, 2008.

[16] M. Zhang, T. Wu, and K. M. Bennett, "Small blob identification in medical images using regional features from optimum scale," *IEEE Transactions on Biomedical Engineering*, vol. 62, no. 4, pp. 1051–1062, 2015.

[17] H. Xu and M. Mandal, "Epidermis segmentation in skin histopathological images based on thickness measurement and k-means algorithm," *EURASIP Journal on Image and Video Processing*, vol. 2015, no. 1, pp. 1–14, 2015.

[18] J. Stegmaier, J. C. Otte, A. Kobitski, A. Bartschat, A. Garcia, G. U. Nienhaus, U. Strähle, and R. Mikut, "Fast segmentation of stained nuclei in terabyte-scale, time resolved 3d microscopy image stacks," *PloS one*, vol. 9, no. 2, p. e90036, 2014.

[19] D. Comaniciu and P. Meer, "Mean shift: A robust approach toward feature space analysis," *IEEE Transactions on Pattern Analysis and Machine Intelligence*, vol. 24, no. 5, pp. 603–619, 2002.